Volume 10
Number 11
21 March 2022
Pages 5653–6252

Journal of Materials Chemistry A

Materials for energy and sustainability

rsc.li/materials-a

Themed issue: Single-Atom Catalysis

ISSN 2050-7488

ROYAL SOCIETY OF CHEMISTRY

PAPER

Jeong Young Park, Chunjoong Kim, Young-Sang Yu, Hyun You Kim *et al.*
Enhancing the inherent catalytic activity and stability of TiO_2 supported Pt single-atoms at CeO_x–TiO_2 interfaces

Journal of
Materials Chemistry A

ROYAL SOCIETY
OF CHEMISTRY

PAPER

View Article Online
View Journal | View Issue

Cite this: *J. Mater. Chem. A*, 2022, **10**, 5942

Enhancing the inherent catalytic activity and stability of TiO_2 supported Pt single-atoms at CeO_x–TiO_2 interfaces†

Mi Yoo, ‡[a] Eunji Kang,‡[a] Hyuk Choi,‡[a] Hyunwoo Ha, [a] Hanseul Choi,[bc] Jin-Seok Choi,[d] Kug-Seung Lee, [e] Richard Celestre,[f] David A. Shapiro,[f] Jeong Young Park, *[bc] Chunjoong Kim,*[a] Young-Sang Yu*[fg] and Hyun You Kim *[a]

Single-atoms (SAs) with atomically coordinated reaction centers are considered the next generation of catalysts that can exhibit exceptional catalytic efficiency. However, the general concern about thermodynamic vulnerabilities of SAs questions their practical value. Moreover, whether the inherent catalytic nature of SAs is superior compared with that of larger nanoparticles is still under debate. Here, we address two controversies by a comparative study using two catalysts: Pt/TiO_2 and Pt/CeO_x–TiO_2. Based on a hierarchical study of density functional theory, time-resolved catalysis performance test, *in situ* infrared spectroscopy, and *operando* X-ray absorption spectroscopy, we could unveil the catalytic nature of Pt-SAs and their stability. By utilizing the heterogeneous interface formed between TiO_2 supporting particles and CeO_x clusters formed on the surface of TiO_2, we preferentially synthesized Pt-SAs pinned at the CeO_x–TiO_2 interfaces on CeO_x–TiO_2 hybrid-oxide supports. The strong electronic coupling between the Pt-SAs and the Ce ions at the CeO_x–TiO_2 interfaces enhanced the catalytic activity toward CO oxidation of Pt-SAs and improved the long-term stability under CO oxidation conditions. The CO oxidation activity of Pt-SAs stabilized at CeO_x–TiO_2 was improved by 13.5 times at 200 °C compared with the Pt-SAs on TiO_2. The results present how to easily improve the activity and stability of Pt-SAs using a simple interface control method. Moreover, we demonstrate that the catalytic activity and the stability of Pt-SAs can be monitored through the chemical state of the interfaces. Our study provides comprehensive understanding about the catalytic nature as well as a novel strategy toward applications of Pt-SAs, enabling sustainable use of Pt in heterogeneous catalysts.

Received 19th September 2021
Accepted 27th September 2021

DOI: 10.1039/d1ta08059h

rsc.li/materials-a

Introduction

The overall catalytic performance of an oxide supported metal catalyst is an ensemble of activity, selectivity, and stability. Since the high price of metal catalysts that are typically scarce precious metals hinders the economical use of the catalysts, one of the primary targets is the design of better performing heterogeneous catalysts. The seminal findings on the high catalytic activity of oxide-embedded metal ions[1,2] and sub-nanometer-sized metal clusters[3–5] stimulated the catalysis communities to scrutinize the catalytic nature of the smaller metal species with a higher surface-to-volume ratio. The size-dependent catalytic properties of metal nanoparticles (NPs) have been intensively studied. The unraveled catalytic function of the metal–oxide interfaces of which density is an inverse function of the size of metal NPs[6,7] and the nature of the size-dependent electronic interaction between metal NPs and supporting oxides[8,9] extended our ability toward rational catalyst design with atomic precision.

---

[a] *Department of Materials Science and Engineering, Chungnam National University, Daejeon 34134, Republic of Korea. E-mail: kimhy@cnu.ac.kr; ckim0218@cnu.ac.kr*

[b] *Center for Nanomaterials and Chemical Reactions, Institute for Basic Science (IBS), Daejeon 34141, Republic of Korea. E-mail: jeongypark@kaist.ac.kr*

[c] *Department of Chemistry, Korea Advanced Institute of Science and Technology (KAIST), Daejeon 34141, Republic of Korea*

[d] *KAIST Analysis Center for Research Advancement, Korea Advanced Institute of Science and Technology (KAIST), Daejeon 34141, Republic of Korea*

[e] *Pohang Accelerator Laboratory, Pohang University of Science and Technology, Pohang 37673, Republic of Korea*

[f] *Advanced Light Source, Lawrence Berkeley National Laboratory, Berkeley, California 94720, USA*

[g] *Department of Physics, Chungbuk National University, Cheongju 28644, Republic of Korea. E-mail: youngsang@chungbuk.ac.kr*

† Electronic supplementary information (ESI) available: Detailed experimental and theoretical methods and additional characterization. See DOI: 10.1039/d1ta08059h

‡ These authors contributed equally to this work.

The recent pioneering findings reported by Qiao *et al.*, in which Pt single-atoms (SAs) can be stabilized on an oxide support and utilized for catalytic reaction, brought SA-based catalysts into the framework of conventional catalysis study.[10] The significant research effort on the SA-based catalysts conducted over the last decade proved that SAs ensure enhanced catalytic activity per unit mass of precious metal.[7,10–13] Due to utilization of every individual atom as a well-confined reaction site, SA-based catalysts are considered the ultimate solution for sustainable use of scarce precious metals such as Pt and Au.[12]· In particular, the atomically confined reaction sites provided by SAs homogenize the reaction pathway, thus improving the selectivity.[14,15]

Intuitively, the dense distribution of SAs over the surface of oxide supporting materials leads to the maximum active site density.[13] If the reaction sites provided by an individual SA are catalytically more reactive than those of the larger clusters or NPs, the dense SA-based catalyst ensures both high economic efficiency and high activity.[13,16] However, the general concern about thermodynamic vulnerabilities of SAs questions their practical application regarding the stability under the reaction conditions.[13] Although SAs exhibit good material efficiency owing to their high surface-to-volume ratio, thermodynamic instability of SAs can drive agglomeration of SAs to large clusters or NPs.[13,17]

To synthesize and stabilize dense SAs on a supporting material, specific strong SA binding sites are required, which make SAs stable against thermodynamically driven agglomeration or ripening.[17–19] Recent relevant findings showed that a certain type of structural ensemble can further stabilize the SAs on supporting oxides through a delicate balance between the SA–adsorbate and the SA–support interactions.[18–23] For example, Pt-SAs could be stabilized in the form of planar PtO_4 at the step edges of CeO_2.[24] Li and coworkers directly visualized the disintegration of NPs into SAs caused by the strong thermodynamic stability of the local Pd–N_4 ensemble in the metal–organic framework support by *in situ* transmission electron microscopy (TEM).[21] The consecutive findings reported by the Wang and the Datye groups confirmed that the polyhedral CeO_2 supported Pt-SAs are stable up to 800 °C under the reaction conditions.[23,25,26] Covalent bond formation among under-coordinated Ce^{3+} ions, Pt-SAs, and bridging oxygen ions led to the high thermal stability of Pt-SAs under the harsh conditions.[26] Similar findings were reported by Zhang, Li, Qiao and coworkers in the Pt-SA/FeO_x system, where the Pt-SAs could be successfully stabilized by a strong covalent metal–support interaction (CMSI).[27] Therefore, fine tuning of the support for strong CMSI has attracted great attention as a promising strategy for the synthesis of stable but dense SAs.[18,26,27]

In addition to the attention on structural stability of SAs, recent findings highlighted that the local structural and electronic ensemble of SAs are highly correlated with their catalytic activity.[28–32] A recent report by the Christopher group demonstrated that the catalytic activity of TiO_2 supported Pt-SAs is highly dependent on the local Pt–O(OH) coordination environments.[29] Depending on the pretreatment conditions, they observed prominent shifts in the infrared spectra of adsorbed CO on Pt-SA.[29] Indeed, utilizing oxide supported oxide clusters as a catalyst has been one of the classic approaches in heterogeneous catalysis communities.[33–38] As more metal–oxygen ensembles become available in SA catalysts, atomic-level precise control of the SA–oxygen ensembles accompanied by the electronic structural change of SAs[29–32] is widening a route toward rational design of SA-based catalysts from the fundamentals.[39] A successful post-modification of the chemical status of the reactive sites in Pt-SA/CeO_2 was reported by Nie *et al.*, by which the catalytic nature of pre-synthesized Pt-SAs can be further optimized toward specific chemical reactions.[25]

Besides, catalytic superiority of the inherent catalytic nature between SAs and NPs is still under debate. The report by Stair and coworkers showed that Pt NPs are reactive for both CO oxidation and water-gas shift reaction, while Pt-SAs behave as spectators due to CO poisoning.[40] The Cargnello group recently demonstrated the severe loss of initial activity of Al_2O_3 supported Pd NPs during methane oxidation, which accounts for the decomposition of Pd NPs into SAs.[41] In addition, Corma and coworkers also reported that several oxide supported Pt-SAs become more reactive upon gradual agglomeration into NPs.[42] More reactive catalytic working sites toward hydrogenation, dehydrogenation, and oxidation reactions were consistently observed in the Pt/oxide catalysts with the larger Pt species.[42] If SAs are inherently less reactive than the larger clusters of NPs, the highly acclaimed economic efficiency of SA-based catalysts should be thoroughly assessed again. Since the dynamic structural evolution of the catalysts during specific reactions such as decomposition of NPs[41] and agglomeration of SAs[43] can also occur in the metal–oxygen ensemble, unraveling the inherent catalytic functionality of SAs can guide catalyst optimization.

Herein, the CO oxidation reaction ($CO + O_2 \rightarrow CO_2$) is scrutinized as a probe reaction. We comparatively study the catalytic activity and stability of Pt-SAs using two different catalyst systems, Pt/TiO_2 and Pt/CeO_x–TiO_2, to provide fundamental understanding about the size-dependent catalytic activity of TiO_2 supported Pt catalysts and confirm the stabilization of Pt-SAs by CMSI-based Pt–oxide interface confinement. The hierarchical protocol of density functional theory (DFT) calculation, time-resolved catalyst performance test, temperature-resolved diffuse reflectance infrared spectroscopy (DRIFTS) analysis, and *operando* synchrotron-based X-ray absorption spectroscopy (XAS) study enabled us to unveil the catalytic nature and stability of Pt-SAs. Furthermore, we present the record-high specific rate and excellent long-term stability of Pt-SAs confined at the CeO_x–TiO_2 interfaces toward CO oxidation. Our study provides comprehensive understanding about the catalytic nature as well as a novel strategy toward applications of Pt-SA-based catalysts, ultimately leading to the sustainable use of Pt in heterogeneous catalytic reactions.

Results and discussion

Structural analysis of the as-synthesized Pt/TiO_2 and Pt/CeO_x–TiO_2 catalysts

We synthesized two types of Pt catalyst supported on conventional TiO_2 oxide powder (hereafter referred to as *n*PT, where *n* indicates the amount of Pt-loading in wt%) or on CeO_x–TiO_2 hybrid oxide powder (hereafter *n*PCT). The CeO_x–TiO_2 hybrid oxide support was prepared by deposition of 1 wt% of Ce ions on the surface of TiO_2 powder (diameter ≈ 25 nm) followed by oxidation, where separated dense CeO_x clusters were uniformly distributed on the surface of TiO_2 powder.[18] The CeO_x–TiO_2 hybrid oxide support with an initial Ce ion content of 1 wt% supplies dense CeO_x–TiO_2 interfaces that facilitate stabilization of most of the supported Pt (0.25 wt%) in the form of SAs (initial Ce to Pt atomic ratio was set to be 3.4 : 1) through strong Pt–Ce electronic interactions.[18] In addition, few Pt-SAs could be observed even in the *n*PCT catalyst with higher Pt-loading ($n = 1.0$ wt%) as determined by scanning transmission electron microscopy (STEM) and XAS analyses.[18] However, in this study, only *n*PT and *n*PCT catalysts with low Pt-loadings ($n = 0.05$, 0.1, and 0.25 wt%) were of interest to exclusively study the inherent catalytic properties of oxide supported Pt-SAs and identify the interplay between the interface and the ensemble effects on the catalytic activity and stability of Pt-SAs.

The STEM images of *n*PT and *n*PCT catalysts ($n = 0.05$, 0.1, and 0.25 wt%) are presented in Fig. 1. The CeO_x–TiO_2 interface drives the preferred generation of Pt-SAs as confirmed in the earlier study.[18] The tiny bright spots that appeared in *n*PCT and 0.05PT catalysts are a distinctive feature of Pt-SAs formed on oxide supports (Fig. 1). While relatively larger Pt clusters with a sub-nanometer size existed in the 0.10PT and 0.25PT systems, such large-sized Pt clusters were not observed in all *n*PCT catalysts, indicating that the CeO_x–TiO_2 interfaces successfully stabilized the supplied Pt into Pt-SAs. The deconvoluted X-ray photoelectron spectroscopy (XPS) spectra agreed well with the what was observed in STEM images. No metallic Pt (Pt^0) was detected in 0.05PT, 0.05PCT, and 0.10PCT catalysts (Fig. S1 and Table S1 in the ESI†), which means that all supplied Pt was atomically dispersed on the surface of TiO_2 (0.05PT) or CeO_x–TiO_2 (0.05PCT and 0.10PCT).

Size dependent catalytic activity in *n*PT: deactivated Pt-SA–TiO_2 interfaces

The temperature-programmed CO conversion profiles (light-off curves) and the corresponding Arrhenius plots of *n*PT catalysts are presented in Fig. 2a and b. Clear size-dependency is observed in the catalytic activities toward CO oxidation. Interestingly, 0.05PT revealed a significant increase in the apparent activation energy barrier for CO oxidation, E_{act}, compared with 0.25PT ($E_{act} = 1.22$ eV for 0.05PT *vs.* $E_{act} = 0.69$ eV for 0.25PT). Such increase in E_{act} confirms that the smaller Pt-species in 0.05PT, Pt-SAs, is less reactive for CO oxidation than the larger Pt-species in 0.25PT, Pt-NPs (Fig. 2a). As a result, the light-off curve of 0.05PT is shifted to a higher temperature region from that of 0.25PT (Fig. 2b). These prominent kinetic data concurrently support the view that the Pt-SAs supported on TiO_2 are inferior to the larger Pt clusters for CO oxidation. Furthermore, the remarkable increase in E_{act} of 0.05PT suggests that the chemical activity of the Pt-SA–TiO_2 interface toward CO oxidation differs from that of the Pt-NP–TiO_2 interface.

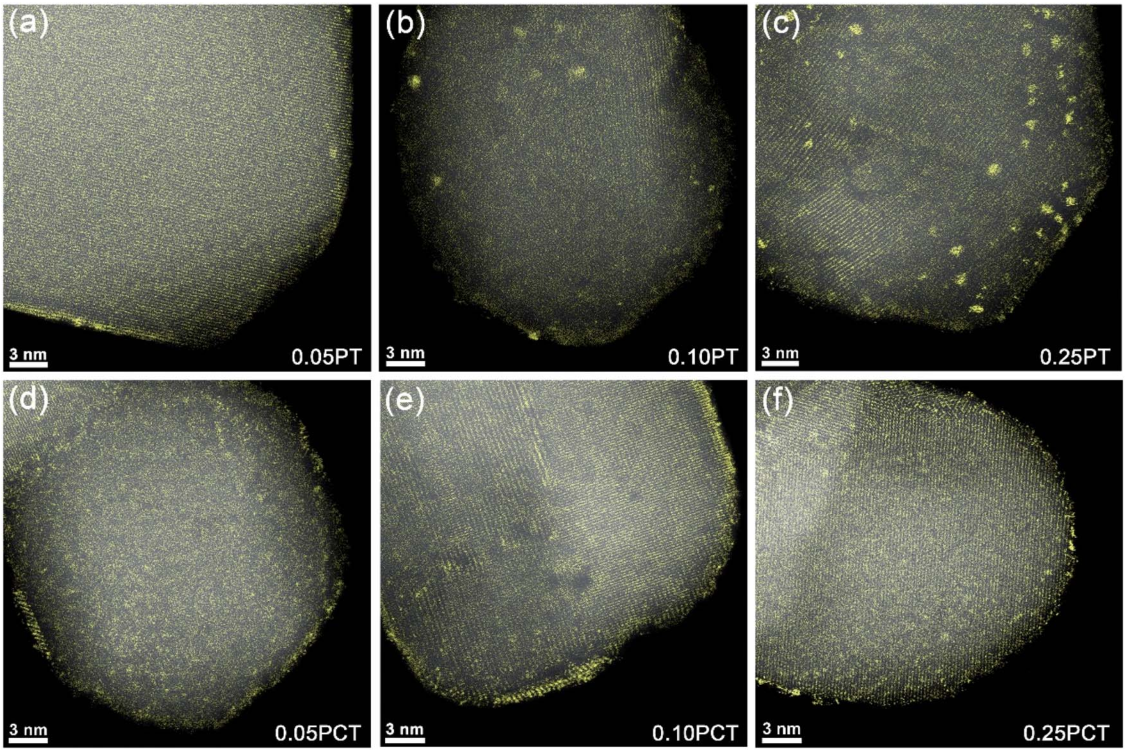

Fig. 1 High-angle annular dark-field (HAADF) STEM images of *n*PT and *n*PCT catalysts with $n = 0.05$, 0.1, and 0.25 wt%. (a) 0.05PT, (b) 0.10PT, (c) 0.25PT, (d) 0.05PCT, (e) 0.10PCT, and (f) 0.25PCT.

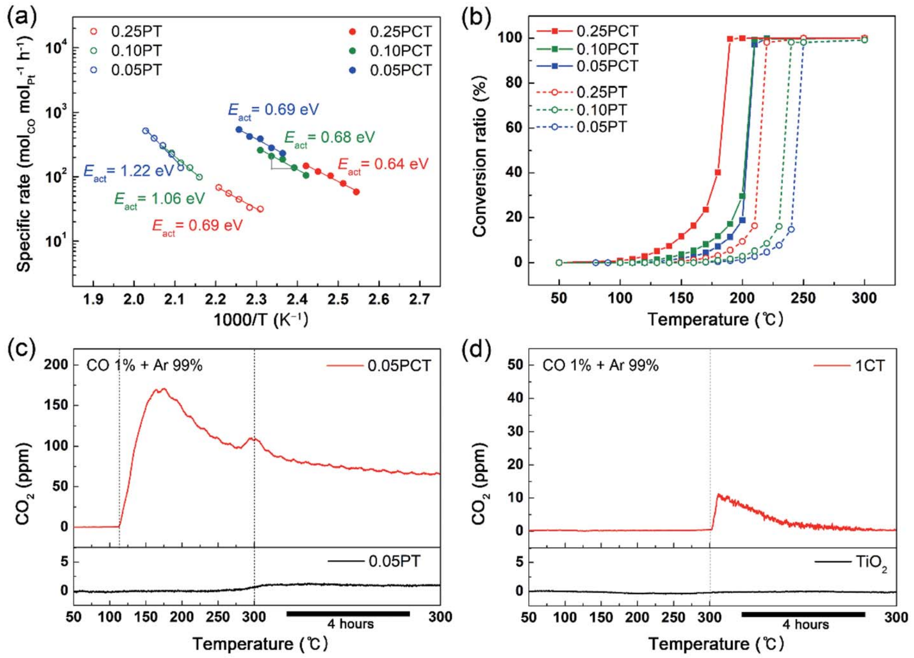

Fig. 2 CO oxidation performance of *n*PT and *n*PCT catalysts. (a) Pt size dependent apparent activation energy barrier, E_{act}, of *n*PT and *n*PCT catalysts. The *n*PCT catalysts in which the CeO_x–TiO_2 interfaces create the well distributed Pt-SAs show similar E_{act} values. However, the E_{act} of *n*PT catalysts is significantly increased upon formation of Pt-SAs on TiO_2 (0.05PT). (b) Temperature-programmed CO conversion profiles (light-off curve) of *n*PT and *n*PCT catalysts. (c) CO-TPR analysis results of 0.05PCT and 0.05PT. (d) CO-TPR analysis results of CeO_x–TiO_2 and TiO_2 support powders.

Because the oxygen-release ability of the metal–oxide interface is directly related to the catalytic activity of the interface during the oxidation reaction,[44–46] we calculated the oxygen vacancy formation energy, E_{vac}, of two different Pt/TiO_2 models, Pt_1/TiO_2 and Pt_9/TiO_2, which closely resemble the Pt-SAs and clusters (or NPs) supported on TiO_2, respectively (Fig. 3a and b). The DFT-calculated E_{vac} of Pt_1/TiO_2 (E_{vac} = 3.65 eV), which is higher than that of Pt_9/TiO_2 (E_{vac} = 2.20 eV), explicitly indicates that the interfacial oxygen of Pt_1/TiO_2 is less reactive. In turn, the higher CO_2 desorption energy of Pt_1/TiO_2 (E_{des} = 2.91 eV) than Pt_9/TiO_2 (E_{des} = 1.28 eV) can explain the trend expected from E_{vac} values. Lastly, the calculated Pt–TiO_2 interaction energy is three times greater in Pt_1/TiO_2 (−2.90 eV/Pt atom) compared with that in Pt_9/TiO_2 (−0.77 eV/Pt atom). All in all, the lattice oxygen ion is strongly bound to the Pt-SA of Pt_1/TiO_2, and is thus reluctant to oxidize Pt–CO*. Our experimental and theoretical results on the relative catalytic inferiority of TiO_2 supported Pt-SAs to the larger Pt clusters are consistent with previous reports which identified the CO-poisoning vulnerabilities of the Pt-SAs under CO oxidation conditions[40] and the deactivation of the Al_2O_3 supported Pd NPs upon decomposition into SAs.[41] An inverse relationship between CO oxidation activity and the diameter of ceria supported Pt NPs larger than 1.6 nm was also reported by Cargnello *et al.*[6] The smaller the NPs, the greater the turnover frequency (TOF), which is attributed to the higher density of the interfacial Pt atoms that work as reaction centers in the smaller NPs.[6] In contrast to the general consensus that SAs with the maximized metal–oxide interface density deliver high activity and improved material efficiency, especially for interface-mediated catalytic reactions,[12,13] our results predict that the decrease in the activity at the interfaces between Pt-SAs and TiO_2 causes the catalytic performance of TiO_2 supported Pt-SAs to deteriorate. Because the inherent catalytic activity of the Pt–TiO_2 interface of 0.05PT is lower than that of 0.25PT, we hypothesize that there would be a critical Pt cluster size at which the mass normalized specific catalytic activity of Pt reaches the maximum. However, the CO oxidation activity of TiO_2 supported Pt-SAs was optimized by pretreatment[29] and the steam-treated Pt-SAs on CeO_2 exhibited enhanced low-temperature activity toward CO oxidation.[25] Therefore, we note that our findings on the relative catalytic inferiority of Pt-SAs in 0.05PT compared with Pt-NPs in 0.25PT should not be overrated as a general principle. Depending on the reaction, the relative catalytic superiority between Pt-SAs and Pt-NPs supported on TiO_2 could be reversed.

Catalytic enhancement of Pt-SAs at CeO_x–TiO_2 interfaces

In contrast, consistent E_{act} values were obtained over three *n*PCT catalysts (Fig. 2a). This implies that the *n*PCT catalysts supply the same kind of major reaction site for CO oxidation albeit with different Pt-loadings. Because of the relatively lower E_{act} values of *n*PCT than those of *n*PT (Fig. 2a), the *n*PCT catalysts completed CO oxidation at a lower reaction temperature (Fig. 2b). Based on the STEM images (Fig. 1d–f) and the kinetic data (Fig. 2a and b), it is strongly believed that the same kind of Pt-SA stabilized at the CeO_x–TiO_2 interfaces but with different Pt-SA densities was formed over the three *n*PCT catalysts. Our

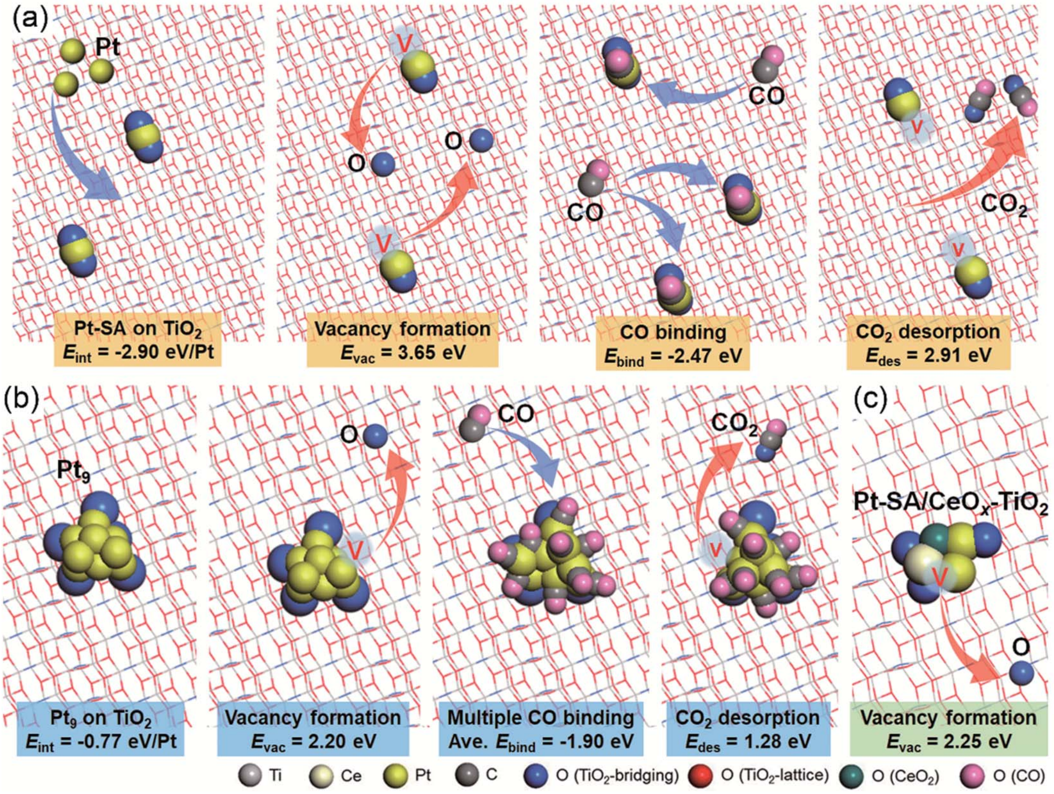

Fig. 3 Long-term CO DFT-estimated interface chemistry of Pt catalysts. (a) Pt-SA on TiO_2, (b) Pt_9 on TiO_2, and (c) Pt-SA on CeO_x–TiO_2. The E_{int} denotes the normalized Pt–TiO_2 interaction energy. E_{vac} and E_{des} correspond to the energy of oxygen vacancy formation and the energy of CO_2 desorption (production), respectively. E_{bind} is the energy of CO binding on Pt. The averaged E_{bind} of total 9 CO molecules is presented in (b).

findings confirm that intensive density control of Pt-SAs is available at the CeO_x–TiO_2 interface. The XPS spectra show the appearance of Pt^0 when Pt loading reaches 0.25 wt%, *i.e.* 0.25PCT (Fig. S1 and Table S1 in the ESI†), suggesting that 0.25 wt% is the upper-limit of Pt-loading for preferential formation of Pt-SAs on CeO_x–TiO_2 hybrid oxide supports. Additional CO temperature programmed reaction (CO-TPR) analysis was conducted on 0.05PCT with a gas mixture (1 vol% of CO and 99 vol% of Ar). The use of testing gas without oxygen can identify the mechanism as confirmed in our previous study.[18] CO-TPR confirmed that the Pt-CeO_x–TiO_2 interfaces of 0.05PCT vigorously supplied oxygen for CO oxidation at temperatures above 110 °C, confirming the operation of the interface-mediated Mars–van Krevelen (MvK) mechanism (Fig. 2c). The DFT-calculated schematic diagram of the MvK type CO oxidation pathway catalyzed by a Pt/CeO_x–TiO_2 model is presented in Fig. S2 in the ESI†. Considering the lower E_{vac} in the Pt-SA/CeO_x–TiO_2 model catalyst (2.25 eV) than that of Pt_1/TiO_2 (3.65 eV) (Fig. 3a and c), the interfacial oxygen in 0.05PCT is more reactive. On the other hand, the Pt–TiO_2 interface in 0.05PT was completely inactive even up to 200 °C and little CO_2 was produced at temperatures above 250 °C (Fig. 2c). Interestingly, the rapid CO_2 production and quick fading of the CeO_x–TiO_2 support powder in the CO-TPR profile (without Pt, Fig. 2d) support the view that the CeO_x–TiO_2 interfaces work as the structurally and chemically well-regulated homogeneous oxygen supply sites. Meanwhile, CO_2 production was not observed in TiO_2 powder (Fig. 2d). Because CeO_x alone does not strongly bind CO,[47] the continuous CO_2 production tail in 0.05PCT during constant temperature CO-TPR performed at 300 °C (Fig. 2c) indicates that the Pt–CeO_x–TiO_2 interface is the oxygen supply gateway for oxidation of Pt–CO*. The Pt–CeO_x–TiO_2 interfaces trigger continuous oxygen supply from TiO_2 under CO-TPR conditions (refer to Fig. 2c and d). The consistent positive order of reaction values with CO of 0.05PCT (0.39) and 0.25PCT (0.34) shows that the reaction sites in 0.05PCT and 0.25PCT are catalytically identical and resistant to CO-poisoning (Fig. S3a and b in the ESI†). On the other hand, the highly negative order of reaction found in 0.05PT (−0.67) confirms that the Pt-SAs in 0.05PT are strongly poisoned by CO (Fig. S3c and d in the ESI†). The theoretical rate map (Fig. S4 in the ESI†) was derived by microkinetic modeling based on DFT-calculated energetics of the MvK type of CO oxidation. The rate map demonstrated that Pt-SAs at the CeO_x–TiO_2 interfaces facilitate CO oxidation at temperatures above 100 °C. The rapid increase in the reaction rate at around 200 °C reproduces the experimental behavior of 0.05PCT presented in the light-off profile (Fig. 2b).

The site normalized reaction rate *vs.* reaction temperature profile of 0.05PT showed that the overall reaction temperature was retarded to the higher temperature from that of 0.05PCT due to the higher E_{act} of 0.05PT (Fig. S5 in the ESI†). The inherent catalytic activity of 0.05PCT is 13.5 times greater than that of 0.05PT at 200 °C, corroborating the excellent activating power of the CeO_x–TiO_2 interfaces. The excellent enhancing effect of the Pt–CeO_x–TiO_2 interfaces boosts the specific CO oxidation rate of 0.05PCT and 0.10PCT, and therefore the TOF of 0.05PCT exceeds most of the literature-reported data points (Table S3 in the ESI†). However, it should be noted that the TOF can be highly influenced by the catalyst test conditions such as space velocity, reactant concentration, and temperature at which TOF is estimated.

Along with recent findings on atomic-precision optimization of the interfaces between metal SAs and oxide supporting materials followed by the enhancement in both catalytic activity and stability of SAs,[23–27,29–32,48–50] our findings on *n*PCT catalysts also demonstrate that the specific Pt–CeO_x–TiO_2 interface ensemble regulates the reaction pathway and activates Pt-SAs. The chemical accessibility of the interfacial oxygen ions at the vicinity of Pt-SAs can be controlled by pre- or post-treatment processes,[25,29] therefore the catalytic performance of 0.05PCT can be further improved through the optimization of Pt–CeO_x–TiO_2 interfaces. The relatively reactive oxygen species with the lower E_{vac} in CeO_x chains or plates[51] can lower the light-off temperature of Pt-SAs.

Because the binding energy, E_{bind}, of a Pt-SA on a pristine TiO_2 (101) surface (−2.94 eV) is weaker than that at the CeO_x–TiO_2 interface (−4.02 eV),[18] the energy for Pt abstraction from the CeO_x–TiO_2 interface is higher than that from TiO_2 (101) (Fig. S6 in the ESI†). Therefore, the CeO_x–TiO_2 interface clearly provides an extra stabilization site for Pt-SAs.

Improved long-term stability of Pt-SAs at CeO_x–TiO_2 interfaces

In order to investigate the stability of catalyst systems, a prolonged reaction test of the 0.05PCT catalyst was carried out under exposure to harsh reaction conditions (1 vol% CO + 4 vol% O_2 + 95 vol% Ar at 300 °C) for up to 24 hours (Fig. 4a, refer to Fig. S7 in the ESI† and discussion therein for the detailed test process). The E_{act} values of 0.05PCT were preserved even after high-temperature and long-term operation. The negligible change in the activation energy barrier is closely related to the structural and catalytic nature of the key reaction site, *i.e.* the Pt–CeO_x–TiO_2 interface, which shows thermodynamic stability even under the harsh reaction environment. Since the physical as well as chemical interactions between Pt-SAs and CeO_x–TiO_2 interfaces were kept unchanged during the reaction conditions, Pt-SAs of the as-synthesized 0.05PCT, 0.05PCT-As, were not agglomerated into larger clusters or NPs but stabilized as the initial structure of the SA. On the other hand, the 0.05PT-As catalyst exposed to the same reaction conditions showed a significant decrease in E_{act} from 1.23 eV to 0.74 eV, even after shorter oxidation of CO (12 hours). It is elucidated that the catalytic nature of the Pt–TiO_2 interface could not be preserved during the long-term CO oxidation test (Fig. 4b). Note that the lowest E_{act} value among the *n*PT catalysts was observed in 0.10PT with the largest Pt species (Fig. 2a). The STEM analysis of 0.05PCT (Fig. 4c, 0.05PCT-12 h) and 0.05PT (Fig. 4d, 0.05PT-12 h) after 12 hours of CO oxidation tests could directly follow the physical change of the Pt-SAs. As expected from the kinetic reaction performance, noticeable agglomeration of Pt-SAs into larger species was not observed in 0.05PCT-12 h. However, the agglomeration of Pt-SAs to NPs was clearly visualized in 0.05PT-12 h, which ultimately leads to the decrease in E_{act} (Fig. 4b). The DFT-calculated energy barriers of Pt-SAs diffusing out from the stable binding site on the TiO_2 (101) and from the CeO_x–TiO_2 interface (Fig. S6 in the ESI†) confirm the enhanced stability of Pt-SAs of 0.05PCT.

The Pt-L_3 edge X-ray absorption near edge structure (XANES) of 0.05PT-As, 0.05PCT-As, 0.05PCT-24 h, and 0.05PT-24 h and the corresponding XANES fitting results are presented in Fig. 5a and Table S2 in the ESI†, respectively. The XANES analysis results clearly confirm that pristine Pt-SAs in 0.05PT-As and 0.05PCT-As show different mechanistic behaviors during the long-term reaction. The significant increase of the metallic Pt in 0.05PT-24 h upon long-term reaction supports the view that the Pt-SAs in 0.05PT-As were agglomerated into Pt clusters or nanoparticles. However, Pt agglomeration was not observed in 0.05PCT-24 h, ensuring the excellent long-term stability of Pt-SAs at the CeO_x–TiO_2 interfaces.

Fig. 5b shows the DRIFTS spectra of 0.05PCT-24 h and 0.05PT-24 h. Indeed, the DRIFTS spectra clearly cross-confirmed the core findings of our study that Pt-SAs in 0.05PCT are stable under the reaction conditions. The exclusively observed CO-stretch peaks at 2103 and 2113 cm^{-1} in 0.05PCT-24 h confirm that CO molecules were adsorbed on top of Pt-SAs (Pt-SA–CO*).[25,29,31,52] On the other hand, the red-shifted major peaks at 2089, 2073, and 2049 cm^{-1} in 0.05PT-24 h indicate that Pt-SAs in 0.05PT-As were agglomerated into clusters and particles during 24 hours of continuous reaction (Pt-NP–CO*).[26,52] Moreover, the temperature-resolved *in situ* DRIFTS spectra of 0.05PCT (Fig. 5c) show the emphasized Pt-SA–CO* peaks which survive up to high temperature. On the other hand, new Pt-NP–CO* peaks emerged upon temperature increase in 0.05PT (Fig. 5d), suggesting that the Pt-SAs in 0.05PT are readily agglomerated into clusters or nanoparticles even at 80 °C due to their instability.

Time-resolved *operando* XAS analysis of long-term stability of Pt-SAs

Among the cutting-edge analysis methods, synchrotron-based *operando* X-ray spectromicroscopy has recently been applied for the direct observation of noble metal SA catalysts.[11,53] The intimate physical and chemical contact between Pt-SAs and CeO_x–TiO_2 interfaces enables an in-depth analysis of the stability of Pt-SAs with time-resolved *operando* XAS monitoring of Ce ions. A schematic diagram shown in Fig. 6a and b presents how the Ce^{4+} (or the Ce^{3+}) concentration in an *n*PCT catalyst responds to the structural evolution of Pt-SAs (adapted with permission from The Royal Society of Chemistry).[18] The synchrotron-based scanning transmission soft X-ray microscopy (STXM) combined with a liquid-flowing nanoreactor could trace the spatiotemporally resolved chemical evolution of Ce ions during the reaction with Pt-precursor solution. The detailed experimental conditions are available in our previous

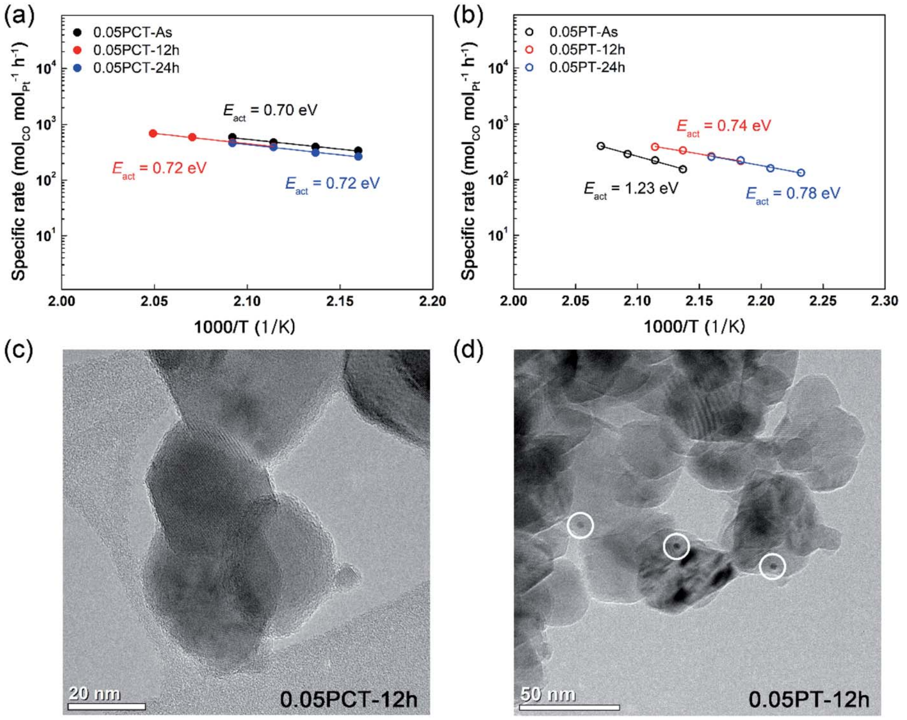

Fig. 4 Long-term CO oxidation test results. The E_{act} of (a) 0.05PCT and (b) 0.05PT catalysts measured before and after the long-term high temperature reaction tests (1 vol% CO + 4 vol% O_2 + 95 vol% Ar at 300 °C). STEM images of (c) 0.05PCT and (d) 0.05PT catalysts after 12 hours of CO oxidation. White circles in (d) represent Pt NPs (diameter ≈ 3 nm). Refer to Fig. S7 in the ESI† and discussion therein for the detailed experimental procedure and additional STEM images.

report.[18] As Pt-SAs are being formed at the CeO_x–TiO_2 interfaces, they donate electrons to adjacent Ce ions, resulting in the decrease in the Ce^{4+} concentration of the CeO_x–TiO_2 interface (from stage 1 to stage 3, Fig. 6b). However, once all available CeO_x–TiO_2 interfaces are occupied by Pt-SAs, newly introduced Pt ions are agglomerated to Pt clusters (stage 4, Fig. 6b). In this

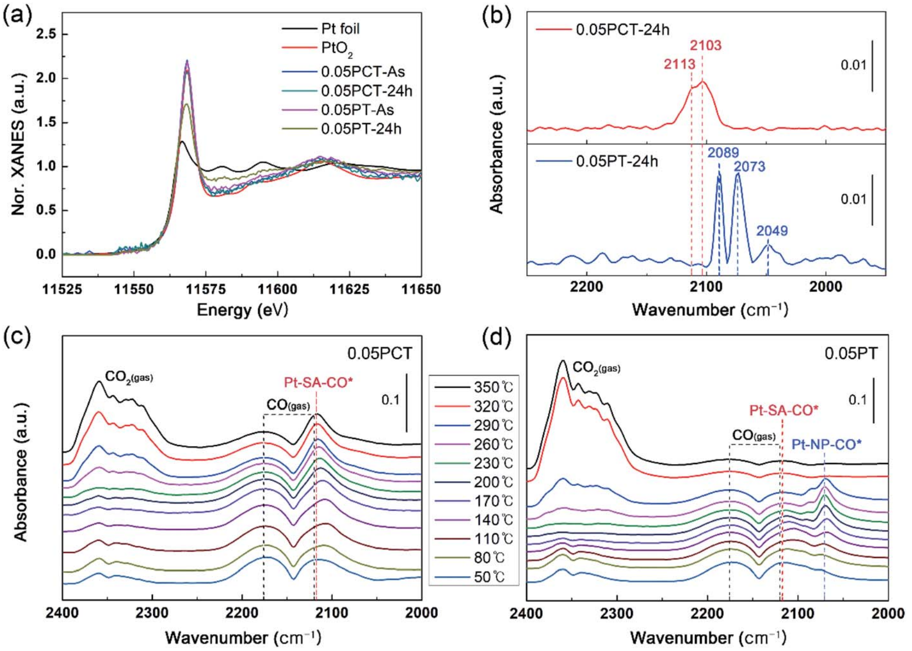

Fig. 5 Spectroscopic evidence of the long-term stability of Pt-SAs in 0.05PCT. (a) Pt-L_3 edge XANES of the as-synthesized 0.05PT and 0.05PCT and used 0.05PCT and 0.05PT for 24 hours of CO oxidation test. (b) DRIFTS spectra of the used 0.05PT and 0.05PCT catalysts for long-term CO oxidation reaction. (c) Temperature-resolved *in situ* DRIFTS spectra of 0.05PCT. (d) Temperature-resolved *in situ* DRIFTS spectra of 0.05PT.

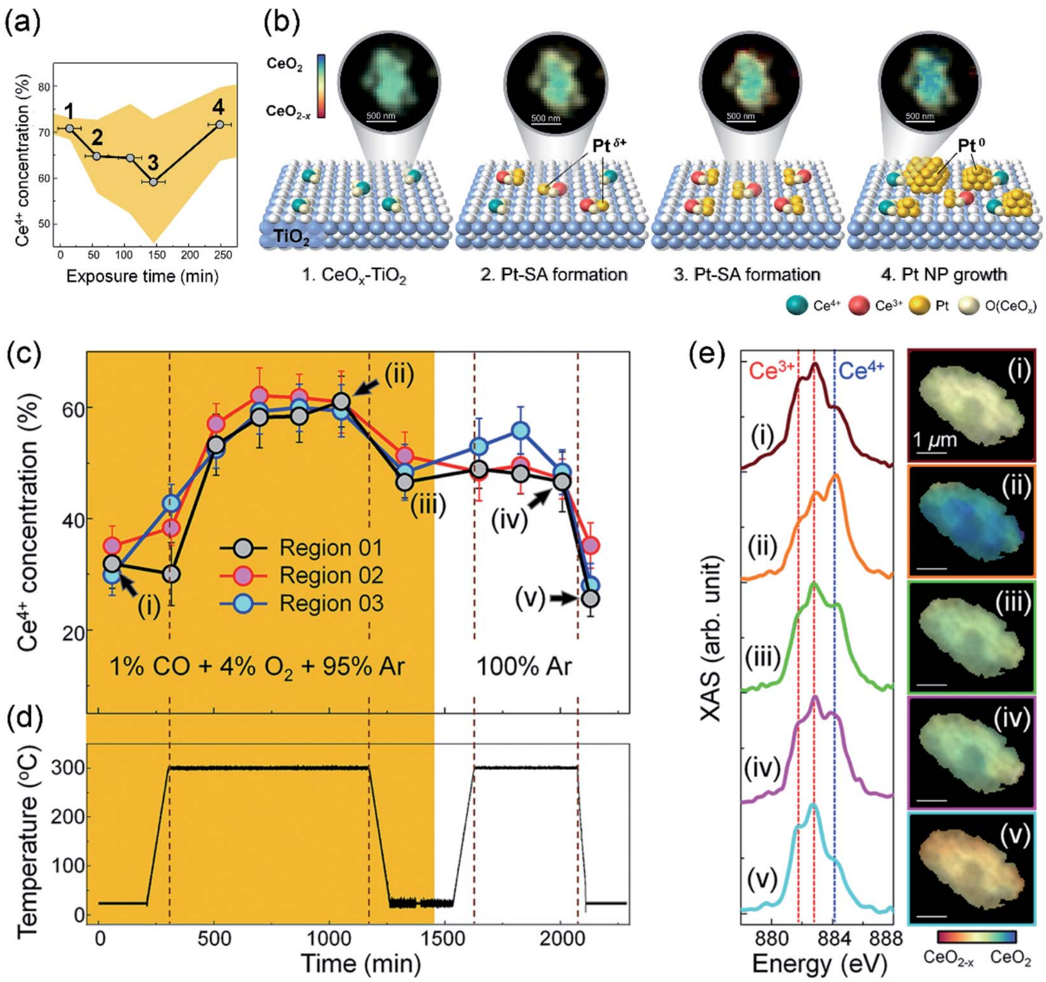

Fig. 6 Spatiotemporally resolved chemical evolution of the *n*PCT catalyst system. (a and b) Schematic diagram showing the correlation between the Pt-size and the Ce^{4+} concentration in the *n*PCT catalyst system. The original *operando* liquid STXM results are adapted from our previous report (adapted with permission from The Royal Society of Chemistry).[18] (a) Ce^{4+} concentration measured *versus* exposure time. The time-dependent Ce^{4+} concentration of the CeO_x–TiO_2 particles with 6 wt% initial Ce-loading is plotted as a function of the exposure time to a circulating solution containing Pt-precursors. The numbered data points in (a) represent the averaged Ce^{4+} concentration over the measured areas. The yellow shaded area indicates the standard deviation. (b) Schematic Pt-SA or cluster models corresponding to the *operando* STXM data points in (a). The increasing areal fraction of the yellowish or reddish region indicates the increasing Ce^{3+}/decreasing Ce^{4+} concentrations upon Pt-SA formation (from stage 1 to stage 3). The original Ce^{4+} concentration is recovered as Pt clusters appear (stage 4). (c–e) *Operando* Ce chemical maps of 0.05PCT under real CO oxidation conditions (1 vol% CO + 4 vol% O_2 + 95 vol% Ar at 300 °C, orange shaded area) and corresponding temperature evolution with a 100 vol% Ar flow (up to 300 °C, white shaded area). (c and d) Averaged Ce^{4+} concentrations from three sample regions with respect to the temperature profile. The error bars in (c) indicate the standard deviation. Chemical information was obtained by linear combination fits of XAS data with reference spectra (Fig. S10 in the ESI†). (e) *Operando* XAS from region 1 (left) and the spatiotemporal chemical evolution (right) specified in (c). Energy positions of M_5-edge absorption features for Ce^{3+} and Ce^{4+} are indicated as dotted red and blue lines, respectively. The fitting results (chemical information) and averaged optical density (morphological information) at each pixel are indicated by a color legend and transparency, respectively. The presence of CeO_2 and CeO_{2-x} is denoted by blue and red colors, respectively.

stage, the number of electrons donated from Pt ions to Ce ions decreases, and finally the Ce^{4+} concentration is recovered almost to the initial value. Therefore, the *operando* STXM observation provides spatiotemporal information on Ce ions that can be applied to track the structural evolution of Pt-SAs under the catalytic reaction conditions and consequently the long-term structural stability of Pt-SAs.[18]

To monitor the potential physicochemical evolution of Pt-SAs of 0.05PCT at the elevated temperature, we performed *operando* STXM analysis (refer to the Methods section and Fig. S8 in the ESI† for more details) on the 0.05PCT catalyst under an inert reaction environment, with a 100 vol% Ar flow at 300 °C for 14 hours. The temperature- and time-dependent overall compositions measured over the three separated sample regions consistently proved that the Ce^{4+} concentration of 0.05PCT did not significantly change during the long-term exposure to Ar at 300 °C (Fig. S9 in the ESI†). Considering that the 0.05PCT catalyst completely converted the supplied CO to CO_2 at temperatures above 200 °C (T_{100}), the negligible change of Ce^{4+} under the environmental conditions of the nanoreactor corroborates the excellent structural stability of the Pt-SAs at the CeO_x–TiO_2 interfaces even at high temperature. Moreover, the electronic state of the Pt–CeO_x–TiO_2 interface, which critically contributes to the chemical activity of the interface, was well preserved during the measurement, again highlighting the high catalytic consistency of our 0.05PCT catalyst.

Based on the long-term physical and chemical stability of Pt-SAs in 0.05PCT under the inert Ar atmosphere at 300 °C, we exposed the 0.05PCT catalyst to the real CO oxidation conditions (1 vol% CO + 4 vol% O_2 + 95 vol% Ar at 300 °C). Interestingly, the *operando* STXM analysis observation (Fig. 6c–e and S11 in the ESI†) showed the rapidly increasing Ce^{4+} concentration with increasing exposure time. If Pt-SAs of 0.05PCT are clustered during the high-temperature CO oxidation reaction, the larger Pt clusters do not donate as much electrons as Pt-SAs do to adjacent Ce ions (Fig. 6b), in turn leading to the increase of the Ce^{4+} concentration. However, after cooling down to room temperature followed by 4 hours of additional stabilization and subsequently 5 hours of high-temperature Ar-treatment processes at 300 °C, the Ce^{4+} concentration of 0.05PCT was decreased again and completely recovered to the initial value. Because the 0.05PCT catalyst did not show any notable change in Ce^{4+} concentration during the long-term heat treatment under the 100 vol% Ar conditions (Fig. S9 in the ESI†), we are convinced that the decreasing Ce^{4+} concentration observed during the second stage heat treatment with pure Ar in Fig. 6c and d did not originate from the structural evolution of Pt-SAs. Rather, because the 0.05PCT catalyst was exposed to oxygen-rich reaction conditions ($CO : O_2 = 1 : 4$) during the long-term reaction test, excess oxygen molecules were adsorbed on the reduced Ce^{3+} ions and oxidized them to Ce^{4+} ions. In addition, similar trends in the control groups where dose damage was minimized confirmed that the beam-induced damage on the sample[54] was negligible (Fig. S12 in the ESI†).

In our previous *operando* gas phase XAS analysis performed on 0.25PCT, we exposed the catalyst to a stream of 7 vol% CO + 93 vol% Ar and elevated the reaction temperature from room temperature to 160 °C.[18] The result showed that the Ce^{4+}/Ce^{3+} ratio was gradually decreased upon exposure to CO as a result of oxygen vacancy formation,[18,44,45] indicating the operation of the MvK type CO oxidation at the Pt–CeO_x–TiO_2 interfaces. The original Ce^{4+}/Ce^{3+} ratio was recovered as the catalyst was cooled down and exposed to air.[18] Meanwhile, our current finding that the Ce^{4+}/Ce^{3+} ratio increased during the high temperature CO oxidation predicts that the oxygen vacancies at the Pt–CeO_x–TiO_2 interfaces, which are generally formed upon CO_2 production, were rapidly healed by O_2 under the oxygen-rich reaction conditions. The continuously decreasing Ce^{4+} concentration observed during the second heat treatment stage in Fig. 6c confirms that these chemisorbed oxygen molecules were gradually desorbed. The control group samples exhibited the same trend confirming the reliability of the data points. Our *operando* gas XAS analysis results corroborate the excellent physicochemical stability of Pt-SAs at the CeO_x–TiO_2 interfaces.

Conclusions

Herein, our experimental and theoretical findings evidence the catalytic superiority of Pt-SAs at CeO_x–TiO_2 interfaces in both catalytic activity and long-term stability. We found that the Pt-SAs in 0.05PT were easily poisoned by CO and agglomerated into larger clusters during the CO oxidation reaction. On the other hand, the CeO_x–TiO_2 interface confined Pt-SAs in 0.05PCT facilitated the MvK mechanism during CO oxidation by utilization of oxygen at the Pt–CeO_x–TiO_2 interface, exhibiting a high specific rate. The time-resolved long-term stability test, *in situ* DRIFTS, and *operando* STXM analysis results concurrently confirmed the excellent physicochemical stability of the Pt-SAs at the CeO_x–TiO_2 interfaces. The combined high catalytic activity and stability of Pt-SAs brought about by the CeO_x–TiO_2 interfaces enable extensive design of Pt-SA-based catalysts optimized for the given chemical reactions through fine-tuning of the catalytic function of the interfaces. Moreover, the most efficient catalyst support, CeO_x–TiO_2, is provided, which can ensure the highest catalytic activity and stability of SAs.

Conflicts of interest

There are no conflicts to declare.

Acknowledgements

This work was supported by a National Research Foundation of Korea (NRF) grant funded by the Korean government (Ministry of Science, ICT and Future Planning, MSIP) (2019R1A2C1089256). C. K and H. Y. K are thankful for the support from the Basic Science Research Program through the NRF funded by the Ministry of Education (2021R1A6A1A03043682). C. K. (2017M3D1A1039561) and K. -S. L (2019M3D1A1079309) are thankful for the support from the Creative Materials Discovery Program through the NRF funded by the MSIP. The work of H. C. and J. Y. P. was supported by the Institute for Basic Science (IBS) [IBS-R004]. This research used resources of the Center for Functional Nanomaterials, which is a U. S. DOE Office of Science Facility, and the Scientific Data and Computing Center, a component of the Computational Science Initiative, at Brookhaven National Laboratory under Contract No. DE-SC0012704. Computing time was also provided by the National Institute of Supercomputing and Networking/Korea Institute of Science and Technology Information (KSC-2020-CRE-0259). The work of D. A. S and Y. -S. Y. was supported by the Director, Office of Science, Office of Basic Energy Sciences, of the US Department of Energy (contract no. DE-AC02-05CH11231). This research used resources of the Advanced Light Source, which is a DOE Office of Science User Facility under contract no. DEAC02-05CH11231.

Notes and references

1 Q. Fu, H. Saltsburg and M. Flytzani-Stephanopoulos, *Science*, 2003, **301**, 935–938.

2 E. W. McFarland and H. Metiu, *Chem. Rev.*, 2013, **113**, 4391–4427.

3 A. A. Herzing, C. J. Kiely, A. F. Carley, P. Landon and G. J. Hutchings, *Science*, 2008, **321**, 1331–1335.

4 J. Oliver-Meseguer, J. R. Cabrero-Antonino, I. Domínguez, A. Leyva-Pérez and A. Corma, *Science*, 2012, **338**, 1452–1455.

5 S. Vajda, M. J. Pellin, J. P. Greeley, C. L. Marshall, L. A. Curtiss, G. A. Ballentine, J. W. Elam, S. Catillon-Mucherie, P. C. Redfern, F. Mehmood and P. Zapol, *Nat. Mater.*, 2009, **8**, 213–216.

6 M. Cargnello, V. V. T. Doan-Nguyen, T. R. Gordon, R. E. Diaz, E. A. Stach, R. J. Gorte, P. Fornasiero and C. B. Murray, *Science*, 2013, **341**, 771–773.

7 L. Liu and A. Corma, *Chem. Rev.*, 2018, **118**, 4981–5079.

8 W. E. Kaden, T. Wu, W. A. Kunkel and S. L. Anderson, *Science*, 2009, **326**, 826–829.

9 Y. Lykhach, S. M. Kozlov, T. Skála, A. Tovt, V. Stetsovych, N. Tsud, F. Dvořák, V. Johánek, A. Neitzel, J. Mysliveček, S. Fabris, V. Matolín, K. M. Neyman and J. Libuda, *Nat. Mater.*, 2016, **15**, 284–288.

10 B. Qiao, A. Wang, X. Yang, L. F. Allard, Z. Jiang, Y. Cui, J. Liu, J. Li and T. Zhang, *Nat. Chem.*, 2011, **3**, 634–641.

11 J. Liu, *ACS Catal.*, 2017, **7**, 34–59.

12 A. Wang, J. Li and T. Zhang, *Nat. Rev. Chem.*, 2018, **2**, 65–81.

13 X.-F. Yang, A. Wang, B. Qiao, J. Li, J. Liu and T. Zhang, *Acc. Chem. Res.*, 2013, **46**, 1740–1748.

14 J. Shan, M. Li, L. F. Allard, S. Lee and M. Flytzani-Stephanopoulos, *Nature*, 2017, **551**, 605.

15 L. Lin, S. Yao, R. Gao, X. Liang, Q. Yu, Y. Deng, J. Liu, M. Peng, Z. Jiang, S. Li, Y.-W. Li, X.-D. Wen, W. Zhou and D. Ma, *Nat. Nanotechnol.*, 2019, **14**, 354–361.

16 A. Beniya and S. Higashi, *Nat. Catal.*, 2019, **2**, 590–602.

17 T. W. Hansen, A. T. DeLaRiva, S. R. Challa and A. K. Datye, *Accounts Chem. Res.*, 2013, **46**, 1720–1730.

18 M. Yoo, Y.-S. Yu, H. Ha, S. Lee, J.-S. Choi, S. Oh, E. Kang, H. Choi, H. An, K.-S. Lee, J. Y. Park, R. Celestre, M. A. Marcus, K. Nowrouzi, D. Taube, D. A. Shapiro, W. Jung, C. Kim and H. Y. Kim, *Energy Environ. Sci.*, 2020, **13**, 1231–1239.

19 J.-C. Liu, Y.-G. Wang and J. Li, *J. Am. Chem. Soc.*, 2017, **139**, 6190–6199.

20 Y. G. Wang, D. Mei, V. A. Glezakou, J. Li and R. Rousseau, *Nat. Commun.*, 2015, **6**, 6511.

21 S. Wei, A. Li, J. C. Liu, Z. Li, W. Chen, Y. Gong, Q. Zhang, W. C. Cheong, Y. Wang, L. Zheng, H. Xiao, C. Chen, D. Wang, Q. Peng, L. Gu, X. Han, J. Li and Y. Li, *Nat. Nanotechnol.*, 2018, **13**, 856–861.

22 Y. He, J.-C. Liu, L. Luo, Y.-G. Wang, J. Zhu, Y. Du, J. Li, S. X. Mao and C. Wang, *Proc. Natl. Acad. Sci. U. S. A.*, 2018, **115**, 7700–7705.

23 J. Jones, H. Xiong, A. T. DeLaRiva, E. J. Peterson, H. Pham, S. R. Challa, G. Qi, S. Oh, M. H. Wiebenga, X. I. Pereira Hernández, Y. Wang and A. K. Datye, *Science*, 2016, **353**, 150–154.

24 F. Dvořák, M. Farnesi Camellone, A. Tovt, N.-D. Tran, F. R. Negreiros, M. Vorokhta, T. Skála, I. Matolínová, J. Mysliveček, V. Matolín and S. Fabris, *Nat. Commun.*, 2016, **7**, 10801.

25 L. Nie, D. Mei, H. Xiong, B. Peng, Z. Ren, X. I. P. Hernandez, A. DeLaRiva, M. Wang, M. H. Engelhard, L. Kovarik, A. K. Datye and Y. Wang, *Science*, 2017, **358**, 1419–1423.

26 D. Kunwar, S. Zhou, A. DeLaRiva, E. J. Peterson, H. Xiong, X. I. Pereira-Hernández, S. C. Purdy, R. ter Veen, H. H. Brongersma, J. T. Miller, H. Hashiguchi, L. Kovarik, S. Lin, H. Guo, Y. Wang and A. K. Datye, *ACS Catal.*, 2019, **9**, 3978–3990.

27 R. Lang, W. Xi, J.-C. Liu, Y.-T. Cui, T. Li, A. F. Lee, F. Chen, Y. Chen, L. Li, L. Li, J. Lin, S. Miao, X. Liu, A.-Q. Wang, X. Wang, J. Luo, B. Qiao, J. Li and T. Zhang, *Nat. Commun.*, 2019, **10**, 234.

28 I. Ro, M. Xu, G. W. Graham, X. Pan and P. Christopher, *ACS Catal.*, 2019, **9**, 10899–10912.

29 L. DeRita, J. Resasco, S. Dai, A. Boubnov, H. V. Thang, A. S. Hoffman, I. Ro, G. W. Graham, S. R. Bare, G. Pacchioni, X. Pan and P. Christopher, *Nat. Mater.*, 2019, **18**, 746–751.

30 G. Spezzati, Y. Su, J. P. Hofmann, A. D. Benavidez, A. T. DeLaRiva, J. McCabe, A. K. Datye and E. J. M. Hensen, *ACS Catal.*, 2017, **7**, 6887–6891.

31 H. Jeong, D. Shin, B.-S. Kim, J. Bae, S. Shin, C. Choe, J. W. Han and H. Lee, *Angew. Chem., Int. Ed.*, 2020, **59**, 20691–20696.

32 H. Wang, J.-X. Liu, L. F. Allard, S. Lee, J. Liu, H. Li, J. Wang, J. Wang, S. H. Oh, W. Li, M. Flytzani-Stephanopoulos, M. Shen, B. R. Goldsmith and M. Yang, *Nat. Commun.*, 2019, **10**, 3808.

33 M. Inomata, K. Mori, A. Miyamoto, T. Ui and Y. Murakami, *J. Phys. Chem.*, 1983, **87**, 754–761.

34 I. E. Wachs, *Dalton Trans.*, 2013, **42**, 11762–11769.

35 H. Y. Kim, H. M. Lee, R. G. S. Pala and H. Metiu, *J. Phys. Chem. C*, 2009, **113**, 16083–16093.

36 G. Deo and I. E. Wachs, *J. Catal.*, 1994, **146**, 323–334.

37 I. E. Wachs, *Catal. Today*, 1996, **27**, 437–455.

38 F. Yang, S. Kundu, A. B. Vidal, J. Graciani, P. J. Ramírez, S. D. Senanayake, D. Stacchiola, J. Evans, P. Liu, J. F. Sanz and J. A. Rodriguez, *Angew. Chem., Int. Ed.*, 2011, **50**, 10198–10202.

39 J. Resasco and P. Christopher, *J. Phys. Chem. Lett.*, 2020, **11**, 10114–10123.

40 K. Ding, A. Gulec, A. M. Johnson, N. M. Schweitzer, G. D. Stucky, L. D. Marks and P. C. Stair, *Science*, 2015, **350**, 189–192.

41 E. D. Goodman, A. C. Johnston-Peck, E. M. Dietze, C. J. Wrasman, A. S. Hoffman, F. Abild-Pedersen, S. R. Bare, P. N. Plessow and M. Cargnello, *Nat. Catal.*, 2019, **2**, 748–755.

42 L. Liu, D. M. Meira, R. Arenal, P. Concepcion, A. V. Puga and A. Corma, *ACS Catal.*, 2019, **9**, 10626–10639.

43 C. Dessal, T. Len, F. Morfin, J.-L. Rousset, M. Aouine, P. Afanasiev and L. Piccolo, *ACS Catal.*, 2019, **9**, 5752–5759.

44 H. Y. Kim and G. Henkelman, *J. Phys. Chem. Lett.*, 2013, **4**, 216–221.

45 H. Ha, S. Yoon, K. An and H. Y. Kim, *ACS Catal.*, 2018, **8**, 11491–11501.

46 Y. Choi, S. K. Cha, H. Ha, S. Lee, H. K. Seo, J. Y. Lee, H. Y. Kim, S. O. Kim and W. Jung, *Nat. Nanotechnol.*, 2019, **14**, 245–251.

47 K. Mudiyanselage, H. Y. Kim, S. D. Senanayake, A. E. Baber, P. Liu and D. Stacchiola, *Phys. Chem. Chem. Phys.*, 2013, **15**, 15856–15862.

48 D. Yan, J. Chen and H. Jia, *Angew. Chem., Int. Ed.*, 2020, **59**, 13562–13567.

49 R. Lang, X. Du, Y. Huang, X. Jiang, Q. Zhang, Y. Guo, K. Liu, B. Qiao, A. Wang and T. Zhang, *Chem. Rev.*, 2020, **120**, 11986–12043.

50 X. I. Pereira-Hernández, A. DeLaRiva, V. Muravev, D. Kunwar, H. Xiong, B. Sudduth, M. Engelhard, L. Kovarik, E. J. M. Hensen, Y. Wang and A. K. Datye, *Nat. Commun.*, 2019, **10**, 1358.

51 H. Y. Kim, M. S. Hybertsen and P. Liu, *Nano Lett.*, 2017, **17**, 348–354.

52 L. DeRita, S. Dai, K. Lopez-Zepeda, N. Pham, G. W. Graham, X. Pan and P. Christopher, *J. Am. Chem. Soc.*, 2017, **139**, 14150–14165.

53 X. Li, X. Yang, J. Zhang, Y. Huang and B. Liu, *ACS Catal.*, 2019, **9**, 2521–2531.

54 E. Paparazzo, G. M. Ingo and N. Zacchetti, *J Vac. Sci. Technol. A*, 1991, **9**, 1416–1420.